Kinetics of atoms, metastable, radiative and ionic species in the nitrogen pink afterglow

2002 J. Phys. D: Appl. Phys. 35 689

(http://iopscience.iop.org/0022-3727/35/7/318)

INSTITUTE OF PHYSICS PUBLISHING JOURNAL OF PHYSICS D: APPLIED PHYSICS

J. Phys. D: Appl. Phys. **35** (2002) 689–699 PII: S0022-3727(02)29863-0

Kinetics of atoms, metastable, radiative and ionic species in the nitrogen pink afterglow

J Levaton[1,2], J Amorim[3], A R Souza[1], D Franco[4] and A Ricard[2]

[1] Laboratório Interdisciplinar de Materiais (LABMAT), Universidade Federal de Santa Catarina, 88040-900 Florianópolis, Brazil
[2] Centre de Physique des Plasmas et leurs Applications (CPAT), Université Paul Sabatier, 31062 Toulouse Cedex, France
[3] Departamento de Física, Instituto Tecnológico de Aeronáutica, Centro Técnico Aeroespacial, 12228-900 São José dos Campos, Brazil
[4] Departamento de Engenharia Ambiental, Universidade Federal de Santa Catarina, PO Box 5039, 88040-970 Florianópolis, Brazil

E-mail: jacques@pg.materials.ufsc.br

Received 17 October 2001
Published 19 March 2002
Online at stacks.iop.org/JPhysD/35/689

Abstract
Direct current N_2 flowing discharges were generated and conditions for the pink afterglow were obtained. Emissions from $N_2(B, C)$ and $N_2^+(B)$ radiative states were studied as a function of pressure, flow rate and post-discharge position. A one-dimensional kinetic model accounting for $N_2(X, v)$, $N_2(A, B, C, a, a', a'')$, $N(^4S)$, $N^+_{1-4}(X)$ and $N_2^+(B)$ species has been developed in order to describe the experimental observations. The analysis on the complete set of processes assumed in this paper has provided possible generation mechanisms for N atoms, $N_2^+(B)$ ions and $N_2(B, C)$ electronically excited states as well as for metastable ones. It has been shown that ionization, excitation and dissociation processes occur simultaneously at the post-discharge region when the vibrational distribution function of $N_2(X, v)$ states heats as resulting from the efficient V–V pumping mechanism, which is very sensitive to pressure conditions. Here, the pink afterglow is described as a non-equilibrium plasma, i.e. ambipolar diffusion for ions and the condition of charge neutrality are assumed.

1. Introduction

The pink afterglow has been known to occur in N_2 flowing discharges for a long time [1]. The phenomenon consists in the appearance of a visible pink luminous region, at post-discharge times of about 10^{-3}–5×10^{-2} s, clearly separated from the discharge by a dark space region [2]. Predominant emitted light originates from $N_2^+(B)$, $N_2(B)$ and $N_2(C)$ states, the ionic emissions being, the first negative system, the dominant ones in the spectrum. Some experimental works concerning the non-radiative species in the pink afterglow can be found. Sadegui *et al* [3] have shown, utilizing the intracavity laser absorption spectroscopy and microwave interferometry techniques, that the $N_2(A)$and electronic (n_e) densities present similar post-discharge spatial profiles as those observed for the radiative species. The same was observed with respect to the neutral ions N_2^+, N_3^+ and N_4^+ [4]. Diamy *et al* [5] and Moritts [6] studied the N atoms density in the pink afterglow for pressures ranging from 2 to 30 Torr. By means of mass spectrometry and NO titration techniques, they have shown that N density presents the same behaviour observed for the other species and that it is sensitive to the pressure parameter. The higher the pressure, the more pronounced is the density peak in the spatial profile. Perhaps, because of this dependence, Mazouffre *et al* [7] did not find similar results concerning the N atom density profile, which was measured by the TALIF technique, since they have worked at 440 Pa. Very recent theoretical works [8–10] propose some possible kinetics mechanisms to explain the pink afterglow. Nowadays, this phenomenon is interpreted as re-ionization and

re-excitation processes originating mainly from the $N_2(X, v)$ states produced in the discharge and transported by the flow to the post-discharge region.

In this paper, we present some experimental results concerning the optical emissions from $N_2(B, C)$ and $N_2^+(B)$ species in a pink afterglow generated by a direct current (DC) source with special emphasis on the pressure parameter. A kinetic model including the calculated $N_2(X, v)$ vibrational distribution function (VDF) is utilized to describe our experimental results. Even though the model is not complete with all possible kinetic processes taking place in the post-discharge, it provides some qualitative agreement with our measurements and with other published ones for all species experimentally studied. In this sense, it may evidence some important kinetic processes in the pink afterglow. In fact, from a detailed analysis on the whole set of processes assumed in this paper, some dominant reaction pathways for the relevant species are proposed.

2. Post-discharge kinetic model

2.1. General description

The kinetic model used in this paper is essentially a one-dimensional relaxation model to describe the post-discharge regime generated by low-pressure N_2 flowing glow discharges. In this sense an initial condition concerning specie densities is required and, from that, a system of rate balance equations for the most relevant neutral and ionic species, coupled to the $N_2(X, v)$ vibrational master equation, is numerically integrated in time. The model provides the $N_2(X, v)$, $N_2(A, B, C, a, a', a'')$, $N(^4S)$, $N^+_{1-4}(X)$ and $N_2^+(B)$ axial populations as a function of time for a discharge vibrational temperature (θ), flow rate (Q), pressure (p) and tube radius (R). Gas (T) and electronic (T_e) temperatures were considered as constants along the post-discharge, whose values are 400 [11] and 2300 K (0.3 eV) [12, 13], respectively. The initial $N_2(X)$ VDF was supposed to be a Boltzmann distribution function at equilibrium temperature (θ).

The coupled system of equations was integrated numerically in Matlab 5.1 environment by an ordinary differential equation (ODE) solver which is appropriate to solve stiff problems [14]. A detailed discussion on the numerical integration method itself is furnished in [15]. The greatest advantage in utilizing this solver is the simplicity of describing and handling the problem. One can be concerned only with the kinetic aspects without directly touching the integration method. Here, the model consistency was checked by verification of the total density of particles, or mass conservation, throughout the integration. For that, a specific set of physical processes was chosen, which does not include sources or sinks, and the total instantaneous mass difference Δt, having as reference value the total mass at $t = 0$, was calculated. It was observed that the mass variation presents a relative error of about 10^{-10} when post-discharge parameters are varied. The initial densities and VDF distribution were not directly calculated from a discharge model for the experimental parameters, but taken from typical ones found in the literature. We think that the most important discrepancy in the model is the initial VDF, considered as a Boltzmann one, which is quite different from the expected one in an N_2 discharge [16]. However, this assumption does not affect the results much, because the VDF evolutes rapidly to a Treanor–Gordiets distribution, as can be seen in the text.

2.2. Kinetics of vibrationally excited states

The processes taken into account for the $N_2(X)$ VDF calculations are described in table 1. We included V–V exchange reactions (V1), V–T exchange reactions for both N_2–N_2 (V2) and N_2–N (V3), vibrational deactivation on the wall (V4) and dissociation promoted by V–V and V–T pumping (V5), the latter occurring into the 46th vibrational pseudolevel [17] with a total dissociation velocity (V_d) [18, 19] which generates a source term ($2 \times V_d$) into the rate balance equation for atomic nitrogen. The N re-association process, occurring on the wall, is supposed to generate $N_2(X, v = 0)$ states with a probability constant $\gamma = 3.2 \times 10^{-4}$ [6]. The last constant was obtained in a mass spectrometry study carried out in the presence of the pink afterglow regime.

The V–T and V–V constants for molecular nitrogen are given in [20]. Rate coefficients $P_{10}(T)$ for V–T reactions are calculated by an analytical expression whose parameters were fitted to compiled experimental data [21]. V–T deactivation rate coefficients for higher levels were calculated by a scaling function which follows the SSH theory [22, 23] as modified by Keck and Carrier [24]. The V–V constants are calculated on the basis of the semiclassical theory [25]. Rate coefficients $P_{10}^{01}(T)$ are taken directly from [25], and for higher levels a scaling function proposed in [26], which approximates the constants to the semiclassical ones, was employed. Inverse reactions were considered and their rate constants calculated from the principle of detailed balance. The rate constants for multiquantum V–T exchange reactions between N_2–N, consisting of the main N_2 vibrational deactivation channel [16, 27, 28], were obtained from a fitted function of data presented in [29]. As in [29, 30], only transitions to the five lower levels were considered ($|v - w| \leqslant 5$) with the same probability for each one. Here, no V–T inverse reactions concerning N_2–N were accounted for. Single quantum molecular vibrational deactivation on the wall was assumed with a deactivation probability $\gamma = 4.5 \times 10^{-4}$ [31]. Energies for $N_2(X, v)$ states were calculated by the Morse oscillator approximation. Other processes influencing the vibrational kinetics were taken into account, such as reactions R19–R23 (table 2) and R26–R30 (table 3). It should be noted that they are V–V exchanging reactions that change considerably the volume kinetic processes. In this sense, these vibrational sinks are taken into account here to avoid overestimated VDFs.

Table 1. Processes concerning $N_2(X, v)$ molecules kinetics.

Reaction		Ref.
(V1)	$N_2(X, v) + N_2(X, w)$ $\leftrightarrow N_2(X, v+1) + N_2(X, w-1)$	[20]
(V2)	$N_2(X, v) + N_2 \leftrightarrow N_2(X, v-1) + N_2$	[20]
(V3)	$N_2(X, v) + N \rightarrow N_2(X, v - \Delta v) + N$	[29]
(V4)	$N_2(X, v) + \text{wall} \rightarrow N_2(X, v-1)$	[31]
(V5)	$N_2(X, v = 45) + N_2(X, w)$ $\rightarrow N + N + N_2(X, w-1)$ $N_2(X, v = 45) + N_2 \rightarrow N + N + N_2$	[18, 19]

2.3. Kinetics of electronically excited states, N atoms and ionic species

Processes accounting for kinetics of states, other than $N_2(X)$ vibrational ones, were grouped into three principal categories. The first one, presented in table 2, concerns processes between nitrogen atoms and molecules. Two- and three-body reactions and also the spontaneous emission phenomenon have been included. Diffusion and interaction with the wall have been considered for $N_2(A)$, $N_2(a)$ and $N_2(a')$ molecules and for N atoms. For the wall loss rate for excited N_2 molecules, one has adopted the formulation described in [29], assuming a γ probability equal to 10^{-3} for $N_2(a)$ and $N_2(a')$ and equal to unity for $N_2(A)$. For N atoms, the surface loss was discussed in a later section.

Some observations concerning reactions in table 2 are carried out. This model does not distinguish different energy states for N atoms. Accordingly, one should consider that N atoms are always in the $N(^4S)$ configuration, even in reaction R6. Possible consequences of this choice do not seem to be so important since the set of reactions does not involve processes linked to higher energy states of N atoms and, also, because $N(^2D, ^2P)$ states are converted to $N(^4S)$ ones in volume and surface reactions. Reaction R22 is proposed given that the $N_2(a)$ state is a singlet with energy very close to the $N_2(a')$ one (see reaction R21) and the mixing between these states is very efficient; see R13 and R16. The $N_2(w)$ state has not been considered due to its weak population as compared with the last ones, even when assuming its production by vibrational pooling mechanisms as R21 and R22. It should be mentioned here that only the vibrational kinetics of the fundamental electronic state has been taken into account.

Table 3 presents some possible processes concerning ionization and ion excitation in an N_2 afterglow. Here, it has been considered that almost all ionization processes generate N_4^+ ions. This assumption should be necessary for reaction R25 if one strictly considers fundamental vibrational levels of $N_2(A)$ and $N_2(a')$ species. Also, it allows us to assume lower vibrational levels in reactions R26–R29. However, for reaction R24, one has assumed N_2^+ ions formation which looks better from the point of view of energy conservation.

The last category of processes, listed in table 4, consists of ionic conversion reactions and ion–electron recombination processes. Reactions R37, R38 and R44 present an important role in this model and will be discussed later. It is worth noting that we have assumed the condition of charge neutrality in the post-discharge regime; hence the electron density is obtained from the sum of ion densities at each instant. As a natural consequence, one assumes ambipolar diffusion for ions. Furthermore, for our experimental set-up, this choice is supported by the selection criterion for ionic diffusion presented in [32], in view of the electronic density measured [12] and calculated [13, 33] in N_2 post-discharges. Products of wall reactions after ambipolar diffusion were considered the same as those of ion–electron recombination reactions R41–R44. The diffusion of $N_2^+(B)$ ions was supposed to be the same as for $N_2^+(X)$.

3. Experimental set-up and operational conditions

The experimental set-up is shown in figure 1. A DC N_2 flowing discharge was generated between two side-armed electrodes 20 cm apart in a pyrex glass tube (1.6 cm i.d., 1.8 cm o.d.). The voltage drop through the positive column was measured by tungsten Langmuir probes. The discharge current was monitored by an amperemeter connected to the circuit. The post-discharge tube, with the same characteristics,

Table 2. Processes concerning N_2 metastable and radiative species kinetics.

	Two-body reaction Three-body reaction Spontaneous emission	k ($cm^6\ s^{-1}$) k ($cm^3\ s^{-1}$) ν (s^{-1})	Ref.
R1	$N_2(A) + N_2(A) \rightarrow N_2(X, v = 0) + N_2(B)$	7.7×10^{-11}	[46]
R2	$N_2(A) + N_2(A) \rightarrow N_2(X, v = 0) + N_2(C)$	1.5×10^{-10}	[47]
R3	$N_2(A) + N_2(A) \rightarrow N_2(X, v = 0) + N(^4S) + N(^4S)$	3×10^{-11}	[29]
R4	$N_2(A) + N_2 \rightarrow N_2 + N_2(X, v = 0)$	3×10^{-16}	[29]
R5	$N_2(A) + N(^4S) \rightarrow N_2(X, v = 0) + N(^4S)$	2×10^{-12}	[29]
R6	$N_2(A) + N(^4S) \rightarrow N_2(X, v = 0) + N(^2P)$	4×10^{-11}	[48]
R7	$N_2(B) + N_2 \rightarrow N_2 + N_2(A)$	2.85×10^{-11}	[19]
R8	$N_2(B) + N_2 \rightarrow N_2 + N_2(X, v = 0)$	1.5×10^{-12}	[19]
R9	$N_2(B) \rightarrow N_2(A) + h\nu$	2.4×10^{5}	[35]
R10	$N + N + N_2 \rightarrow N_2(B) + N_2$	$8.3 \times 10^{-34} \exp(500/T)$	[49]
R11	$N_2(C) + N_2 \rightarrow N_2(a') + N_2$	10^{-11}	[29]
R12	$N_2(C) \rightarrow N_2(B) + h\nu$	2.74×10^{7}	[35]
R13	$N_2(a) + N_2 \rightarrow N_2(a') + N_2$	9.1×10^{-12}	[50]
R14	$N_2(a) \rightarrow N_2(X, v = 0) + h\nu$	1.8×10^{4}	[51]
R15	$N_2(a) \rightarrow N_2(a') + h\nu$	1.91×10^{2}	[52]
R16	$N_2(a') + N_2 \rightarrow N_2(a) + N_2$	$1.82 \times 10^{-11} \exp(-1700/T)$	[29]
R17	$N_2(a') + N_2 \rightarrow N_2(B) + N_2$	1.9×10^{-13}	[53]
R18	$N_2(a'') + N_2 \rightarrow N_2(X, v = 0) + N_2(X, v = 0)$	2.3×10^{-10}	[54]
R19	$N_2(A) + N_2(X, 4 < v < 15) \rightarrow N_2(B, v < 13) + N_2(X, v = 0)$	2×10^{-11}	[19]
R20	$N_2(X, v > 23) + N_2(X, v > 23) \rightarrow N_2(a'') + N_2(X, v = 0)$	1.6×10^{-15}	[55]
R21	$N_2(X, v > 15) + N_2(X, v > 15) \rightarrow N_2(a') + N_2(X, v = 0)$	$2.1 \times 10^{-14} \exp(-700/T)$	[29]
R22	$N_2(X, v > 15) + N_2(X, v > 15) \rightarrow N_2(a) + N_2(X, v = 0)$	$2.1 \times 10^{-14} \exp(-700/T)$	p.w.
R23	$N_2(a') + N_2(X, v > 3) \rightarrow N + N + N_2(X, v = 0)$	10^{-11}	p.w.

Table 3. Processes concerning ionization and ion excitation kinetics.

	Two-body reaction Spontaneous emission	k (cm^3 s^{-1}) ν (s^{-1})	Ref.
R24	$N_2(a') + N_2(a') \rightarrow N_2^+(X) + N_2(X, v = 0) + e$	10^{-11}	[55]
R25	$N_2(A) + N_2(a') \rightarrow N_4^+ + e$	3.2×10^{-12}	[29]
R26	$N_2(X, v > 8) + N_2(a'') \rightarrow N_4^+ + e$	$10^{-11} \exp(-640/T)$	[55]
R27	$N_2(X, v > 24) + N_2(a') \rightarrow N_4^+ + e$	10^{-12}	[42]
R28	$N_2(X, v > 29) + N_2(X, v > 29) \rightarrow N_4^+ + e$	$3.5 \times 10^{-15} \exp(-1160/T)$	[56]
R29	$N_2(X, v > 36) + N_2(A) \rightarrow N_4^+ + e$	10^{-13}	[55]
R30	$N_2^+(X) + N_2(X, v > 11) \rightarrow N_2^+(B) + N_2(X, v = 0)$	$3 \times 10^{-11} \exp(-4.3 \times 10^{-4}(T - 700)/T)$	[56]
R31	$N_2^+(B) \rightarrow N_2^+(X) + h\nu$	1.6×10^7	[35]

Table 4. Processes concerning ion transfers and ion–electron recombination kinetics.

	Two-body reaction Three-body reaction	k (cm^3 s^{-1}) k (cm^6 s^{-1})	Ref.
R32	$N^+ + N_2 + N_2(X, v = 0) \rightarrow N_2 + N_3^+$	$1.7 \times 10^{-29}(300/T)^{2.1}$	[57]
R33	$N^+ + N + N_2 \rightarrow N_2^+ + N_2$	$10^{-29} \times (300/T)$	[42]
R34	$N_2^+ + N \rightarrow N^+ + N_2(X, v = 0)$	$7.2 \times 10^{-13}(T/300)$	[40]
R35	$N_2^+ + N_2 + N_2(X, v = 0) \rightarrow N_4^+ + N_2$	$5.2 \times 10^{-29}(300/T)^{2.2}$	[57]
R36	$N_2^+ + N + N_2 \rightarrow N_3^+ + N_2$	$0.9 \times 10^{-29} \exp(400/T)$	[40]
R37	$N_3^+ + N \rightarrow N_2^+ + N_2(X, v = 0)$	6.6×10^{-11}	[40]
R38	$N_4^+ + N \rightarrow N_3^+ + N_2(X, v = 0)$	10^{-9}	[58]
R39	$N_4^+ + N_2 \rightarrow N_2^+ + N_2 + N_2(X, v = 0)$	$2.1 \times 10^{-16} \exp(T/121)$	[40]
R40	$N_4^+ + N \rightarrow N^+ + N_2(X, v = 0) + N_2(X, v = 0)$	10^{-11}	[40]
R41	$N^+ + e \rightarrow N + h\nu$	3.2×10^{-12}	[59]
R42	$N_2^+ + e \rightarrow N + N$	$1.8 \times 10^{-7}(300/T_e)^{0.39}$	[60]
R43	$N_3^+ + e \rightarrow N + N_2(X, v = 0)$	$2.0 \times 10^{-7}(300/T_e)^{0.5}$	[49]
R44	$N_4^+ + e \rightarrow N_2(C) + N_2(X, v = 0)$	$2.3 \times 10^{-6}(300/T_e)^{0.53}$	[61]

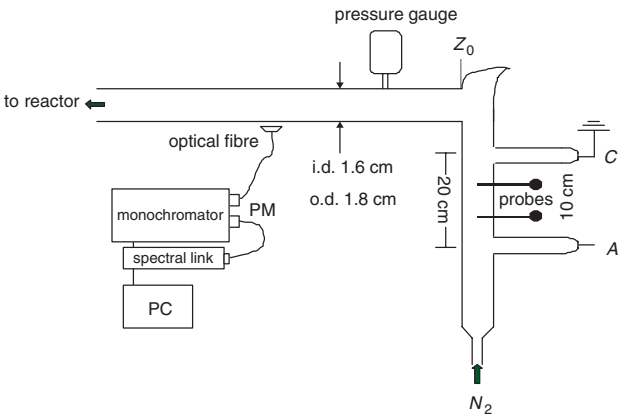

Figure 1. Experimental set-up. A: anode; C: cathode; Z_0: assumed origin of post-discharge.

was assembled transversely to the latter one with the aid of a Wood trap, to avoid discharge light in the post-discharge region. Gas pressure and flow rate were measured by means of a baratron gauge (MKS, 626A) and a mass flow meter (Edwards, EH250), respectively. The N_2 gas utilized was a high-purity gas (99.999%). The glow and afterglow emissions were recorded by means of a monochromator (Jobin-Yvon, HR640, 1200 grooves mm^{-1}) connected to a photomultiplier tube (Hamamatsu, R928). A 0.5 mm diameter optical fibre was utilized to guide the light emitted from several discharge and post-discharge positions. All spectra records were accompanied simultaneously by discharge current and voltage measurements and, from those ones, the reduced electric field and electronic density were determined.

The work conditions were pressure (p) between 3 and 10 Torr, flow rate (Q) between 0.4 and 0.5 Slm^{-1}, 70 mA constant discharge current and voltage (V) between 280 and 510 V. The mean power dissipated by the discharge was varied from 20 to 36 W and the reduced electric field from 5.4 to 2.7×10^{-16} V cm^2 for the pressure range mentioned above. The electronic density was estimated from the current density and drift velocity, which was linearly adjusted as a function of reduced electric field from data presented in [34]. For our conditions, n_e was found between 3.4 and 5.7×10^{10} cm^{-3}.

4. Experimental results

The $N_2^+(B, v = 0, 1)$ ionic and $N_2(C, v = 0, 1)$ electronically excited states were studied by recording spectra in the range of 375–395 nm comprising emissions from the first negative and second positive N_2 systems [35]. The $N_2(B, v = 6–12)$ states were studied by spectral emissions from the first positive system in the range of 570–610 nm. Figure 2 reports the 375–395 nm spectra measured at the end of the positive column and at the beginning of the post-discharge tube ($Z_0 = 2.5 \pm 0.5$ cm from the cathode) for $p = 1$ and 9 Torr. A direct comparison between $N_2^+(B, 0–X, 0)$ emissions, for $p = 9$ Torr, shows a decrease of 3.6 times in peak intensity, and thus in excited ionic nitrogen density, from the end of the positive column to the beginning of the post-discharge (Z_0). When the same analysis is applied to $N_2(C, 0–B, 2)$ intensities, one finds a decrease of 12 times in $N_2(C, 0)$ population. The reduction of both populations clearly results from the EEDF relaxation since their production occurs, directly or indirectly, by electronic impact processes in the discharge. A similar

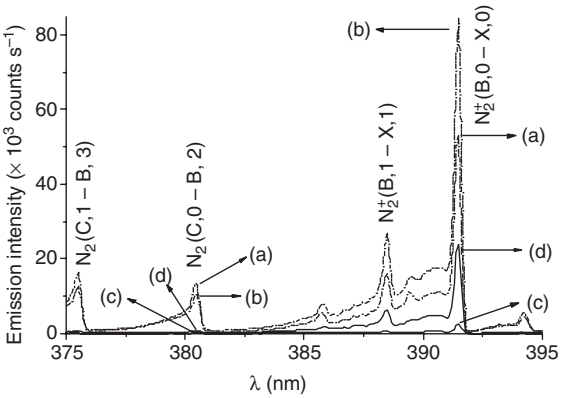

Figure 2. Emission spectra between 375.0 and 395.0 nm recorded in discharge (- - - -), at the end of the positive column, for conditions $Q = 500$ sccm, $I = 70$ mA, $p = 1$ Torr (a) and $p = 9$ Torr (b). The same spectra were recorded at the beginning of the post-discharge tube (——) for $p = 1$ Torr (c) and $p = 9$ Torr (d).

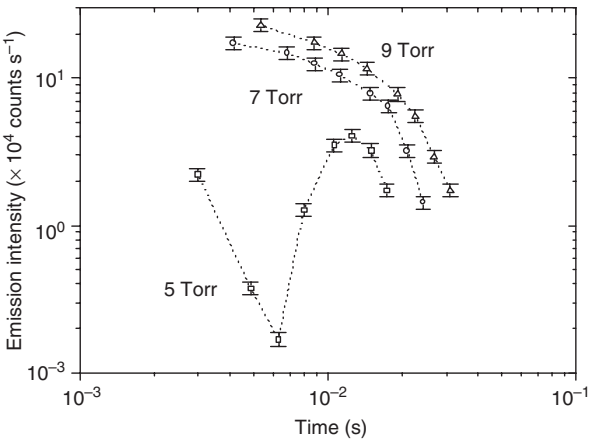

Figure 3. $N_2^+(B, 0–X, 0)$ intensity profile at the post-discharge tube as a function of residence time for conditions $Q = 500$ sccm, $I = 70$ mA, $p = 5$ Torr (□), $p = 7$ Torr (○) and $p = 9$ Torr (△). The residence time was calculated as a function of position for a 400 K fixed temperature along the post-discharge tube of radius $r = 0.8$ cm.

analysis at $p = 1$ Torr shows that $N_2^+(B, 0)$ population decreases 21 times when the discharge peak emission is compared with the post-discharge one. For $N_2(C, 0)$, a decrease of 76 times was measured. It is then verified that $N_2(C, 0)$ density decreases approximately 3.5 times faster than the $N_2^+(B, 0)$ one at both pressures. This probably indicates that similar mechanisms are responsible for $N_2(C)$ and $N_2^+(B)$ emissions at the beginning of the post-discharge tube for a pressure range of 1–9 Torr and that they are amplified as the pressure rises.

After establishing the experimental conditions of the pink afterglow regime, the emissions of $N_2^+(B)$, $N_2(B)$ and $N_2(C)$ states were studied as functions of pressure, flow rate and post-discharge position. The 391.4 nm emission profile along the post-discharge tube for different pressure values is reproduced in figure 3. For a pressure of 5 Torr, the pink afterglow peak occurs at $t \sim 12.5$ ms. As pressure increases, the afterglow volume increases and a considerable change occurs in the emission profile. Figure 4 shows the intensity profiles for 380.5 and 580.4 nm head bands generated by the $N_2(C, 0)$ and

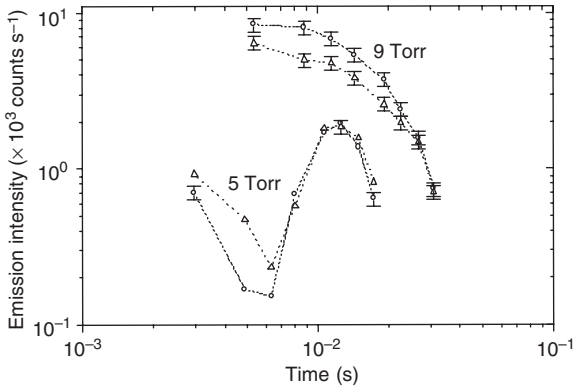

Figure 4. $N_2(B, 11–A, 7)$ intensity (△) and $N_2(C, 0–B, 2)$ intensity (○) z-profiles as in figure 3, but for pressure values of 5 and 9 Torr.

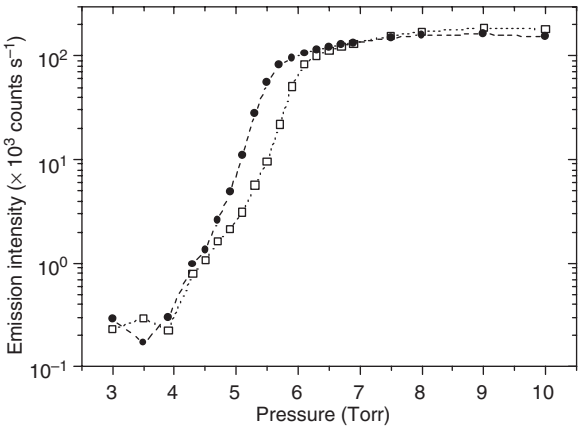

Figure 5. $N_2^+(B, 0–X, 0)$ intensity as a function of pressure at initial post-discharge position $z = Z_0$ for conditions $I = 70$ mA, $Q = 500$ sccm (□) and $Q = 400$ sccm (●).

$N_2(B, 11)$ states, respectively. They are similar to the first ones, for excited ions, apparently indicating a close relation in their generation mechanisms. For the $N_2(B, v)$ emissions, similar profiles coming from the $v = 6$ to $v = 12$ vibrational states were observed.

For our experimental parameters (500 sccm flow rate, 70 mA discharge current and 2 Torr pressure), no light could be visualized along the post-discharge tube. The variation of pressure from 2.0 to 4.0 Torr produced a small pink luminous volume at the end of the post-discharge tube ($z \sim 15$ cm). The further increase in pressure caused the volume displacement towards the beginning of the post-discharge tube, at the same time that it would be enlarged. Roughly at 6.0–7.0 Torr the volume extremity, closer to the discharge, reached the position Z_0 and suddenly the full post-discharge tube was filled with an intense pink afterglow. From this point, a whole intensity increase could be observed until $p = 9$–10 Torr, but the peak position could not be distinguished visually. The described picture and the post-discharge profiles (figures 3 and 4) well match the data presented in figure 5. In this study, the fibre position was fixed at Z_0 and, for each flow rate value, the pressure was varied from 3 to 10 Torr. Care has been taken to remove the discharge light, especially at the low-pressure range where the SLA light is still weak. It is observed for both flow rates that intensity increases by almost three orders

of magnitude when pressure rises from 4 to 7 Torr. The strong dependence of the radiative species on the pressure parameter seems to indicate that $N_2(X, v)$ vibrational states may be their precursors. The vibrational populations of intermediate- and high-energy levels tend to grow, at least, with the square of pressure until the V–T reactions dominate. Furthermore, the higher the pressure, the longer the residence time of the species. So, it is expected that volume reactions, which generate the light in the post-discharge region, be displaced towards shorter positions. Still, it can be observed in figure 5 that for a higher flow rate, the curve is slightly displaced towards higher pressure values. The displacement can be understood as necessary to compensate the decrease in the residence time, because as the flow rate increases, the VDF is cooled. In conclusion, information provided by the experiment strongly supports the assumption that vibrational mechanisms may act as a source for investigated species.

The variation of the discharge vibrational temperature as a function of pressure was calculated for the $N_2(X, v)$ states. This was done by means of the $N_2(C, v)$ relative populations, obtained from the second positive emissions [36], and with the aid of the Franck–Condon factors for the transitions $N_2(X, v) \rightarrow N_2(C, v')$ [35]. A variation from 3650 to 7500 K was found as pressure varies between 1 and 9 Torr. At these pressures, it can be expected that the $N_2(A)$ state influences the $N_2(C)$ vibrational populations and, hence, the calculated vibrational temperature. However, the results obtained can be utilized as an estimation for model running [37].

5. Results of the model—discussion on sensitive reactions

5.1. $N_2(X, v)$ vibrational population

We start presenting the calculated VDFs. For all simulations, the set of initial conditions was kept fixed. The atomic nitrogen density was considered as $7.5 \times 10^{14}\,cm^{-3}$ [6, 33]. The electronic excited states densities were taken from [38], for a discharge residence time on the order of 10^{-2} s, given that our experimental conditions are very close to those assumed there. They are $[N_2(A)] = 10^{12}\,cm^{-3}$, $[N_2(B)] = 5 \times 10^{11}\,cm^{-3}$, $[N_2(C)] = 3 \times 10^{8}\,cm^{-3}$, $[N_2(a')] = 10^{12}\,cm^{-3}$, $[N_2(a)] = 10^{11}\,cm^{-3}$ and $[N_2(a'')] = 10^{10}\,cm^{-3}$. Ionic densities were considered as $[N_2^+(X)] = 5 \times 10^{10}\,cm^{-3}$, $[N^+_{1,3-4}] = 0$ and $[N_2^+(B)] = 5 \times 10^{8}\,cm^{-3}$. Figures 6 and 7 show the distributions for $p = 5$ and 9 Torr, respectively. The heating effect on the VDF is clearly evidenced when pressure rises, noticeably at $t = 10^{-3}$ s, when V–T reactions are still not efficient and the V–V near-resonant pumping mechanism dominates. At $t = 10^{-2}$ s, the curves calculated in the presence of all mechanisms (solid lines) are almost the same for both pressure values. This can be explained by the vibrational quanta consumption for electronic excited species formation and by the increase in the $N–N_2(X, v)$ quenching mechanism generated by extra N atom production via reaction R23.

5.2. Results without excitation by $N_2(X, v)$ pooling reactions

An interesting insight on the role of vibrational states can be achieved comparing modelling with and without the

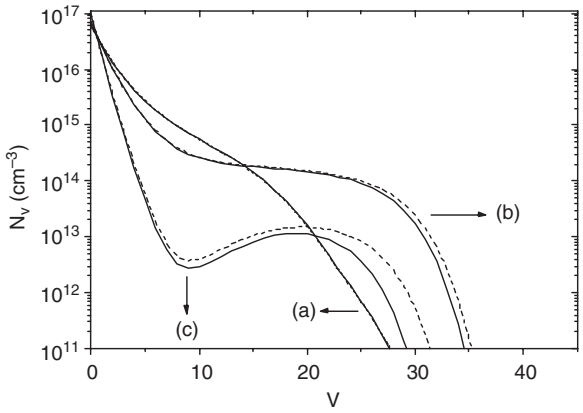

Figure 6. Calculated VDFs for $p = 5$ Torr, $T = 400$ K and $\theta = 6000$ K at (a) 10^{-3}, (b) 10^{-2} and (c) 10^{-1} s. The solid curves represent the VDFs in the presence of all possible mechanisms considered in this paper (see tables 1–4). The dashed curves account only for $N_2(X, v)$ molecules and N atoms mechanisms (see table 1).

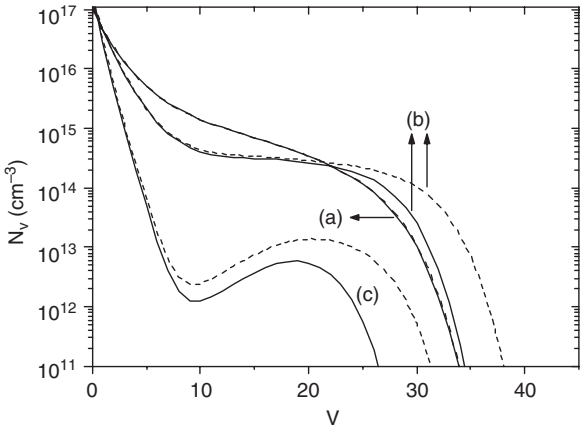

Figure 7. Calculated VDFs, under the same conditions as in figure 6, but for $p = 9$ Torr and $\theta = 7500$ K.

vibrational sources. Initially, these sources (see tables 2 and 3), that populate the metastable, radiative and ionic states, were removed from the model, with the exception of reactions R19 and R30 usually proposed in the literature. Thus, the only source of ionization is assumed to be the pooling reactions (R24 and R25, table 3) among $N_2(A)$ and $N_2(a')$ metastables coming from the discharge. Figure 8 reports the temporal variations of principal electronically excited species in an N_2 afterglow. The initial assumed conditions are the same as those in figure 6. The $[N_2(a'')]$ behaviour reflects the strong quenching mechanism R18. The $N_2(B)$ profile behaves similarly to the $N_2(A)$ one, but presenting a stronger decrease since it is a radiative state. The $N_2(C)$ profile follows that for N_4^+ ions (see reaction R44), which present a slight maximum at $t \sim 2 \times 10^{-6}$ s (see figure 10) resulting from the ionic mixing reactions, especially from reaction R35. It should be remembered that $[N_4^+] = 0$ at $t = 0$. A particularly interesting result concerns the $N_2(a')$ state. Even presenting a long lifetime [35] and a low quenching constant (reaction R17), it is quickly consumed after 10^{-4} s mainly by reaction R17, as can be verified in comparing the consumption frequencies of reactions R17, R24 and R25. At $t = 10^{-3}$ s, which is the characteristic

time for the pink afterglow regime, its density is negligible. In agreement with the latter discussion, the $N_2^+(B)$ profile, shown in the same figure, presents a decreasing monotonic behaviour.

As a conclusion, the calculated profiles for $N_2(B, C)$ and $N_2^+(B)$ species cannot reproduce the experimental ones (see figures 3 and 4) when only reactions R19 and R30 are considered, i.e. if metastable and ionic species are not created in the afterglow. As follows, the remaining vibrational mechanisms are taken into account and their effects are investigated.

5.3. Results with excitation by $N_2(X, v)$ pooling reactions

Figure 9 shows the N_2 excited states for the same initial conditions as assumed before, but the complete set of reactions was allowed in simulations, i.e. including vibrational sources. The $N_2(B)$, $N_2(C)$ and $N_2^+(B)$ radiative states now present a profile with a peak at $t \sim 10^{-2}$ s in good agreement with our experimental data (figures 3 and 4). At time corresponding to the maximum in the curve, the $N_2(a')$ density has risen more than six orders of magnitude as compared with the former profile presented in figure 8. The $N_2(A)$ profile has also changed and a significant increase in its density occurs simultaneously to that of the $N_2(a')$ state. This new picture is in good qualitative agreement with experimental results presented in the literature. As observed by Supiot *et al* [2], the short-lived afterglow (SLA) spatial intensity profiles, generated from the $N_2(B, C)$ and $N_2^+(B)$ states, are similar and present a non-monotonic feature along the post-discharge tube. In those ones, a marked minimum is observed, characterizing the dark space region, followed by the growth in the SLA emissions to a marked maximum. The same was observed by Sadegui *et al* [3] for n_e and $N_2(A)$ density profiles. They have studied the SLA generated by a 433 MHz source in a 3.8 cm inner tube diameter whose dissipated power was 300 W and the pressure was equal to 3.3 Torr. For that, at the SLA maximum, $n_e = 6 \times 10^9\,cm^{-3}$ and $[N_2(A)] = 5 \times 10^{10}\,cm^{-3}$ was found. Assuming this pressure and tube diameter and considering the following initial conditions, $n_e = 1.2 \times 10^{10}\,cm^{-3}$ [11], $[N] = 10^{15}\,cm^{-3}$ [7], $\theta = 10^4$ K [11], $T_{discharge} = 800$ K [11] and other initial values, but the ionic densities which depend on n_e, as indicated in section 5.1, our model predicts, at the SLA maximum, $n_e = 3.5 \times 10^{10}\,cm^{-3}$ and $[N_2(A)] = 7.5 \times 10^{10}\,cm^{-3}$. Bromer and Hesse [4] have shown that the neutral ionic states N_{2-4}^+ also present similar profiles as our results reproduced in figure 9. They have measured, at the SLA maximum with $p = 4.4$ Torr, the ionic density ratios $(N_2^+) : (N_3^+) : (N_4^+) = 1 : 1.9 : 0.64$. The calculated profiles for ions and electron densities are presented in figure 10 under the same conditions as in figure 9. The model predicts that N_3^+ and N_2^+ ionic densities predominate that for N_4^+ in accordance with [4]. At the SLA maximum, the ratios $(N_2^+) : (N_3^+) : (N_4^+)$ are $1 : 5 : 0.35$ and the electronic density is $1.8 \times 10^{10}\,cm^{-3}$. In [10], the rate constant k_{R38} was considered the same as k_{R37}. In this case, for the same conditions as here, N_4^+ and N_3^+ ions predominate the N_2^+ ones, in accordance with [39], and the maximum electronic density is $8 \times 10^9\,cm^{-3}$. Interesting information furnished by the model concerns the initial ionic configuration which seems to play a minor role in the set of initial conditions. As a result of the ionic mixing reactions (table 4), identical ionic profiles for N_{1-4}^+ ions are observed at times longer than 10^{-5} s if the initial electronic density is kept constant. This has been interpreted as a consequence of the equilibrium achieved by ionic mixing reactions. This argues in favour of a simple electronic density experimental estimation as entry for the model.

A further analysis on the mechanisms involving vibrational states, R20–R22 (table 2) and R26–R29 (table 3), was carried out to evidence their contribution to ionization

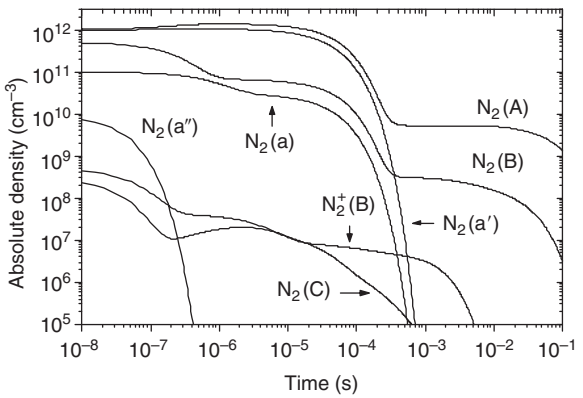

Figure 8. $N_2(A)$, $N_2(B)$, $N_2(C)$, $N_2(a)$, $N_2(a')$, $N_2(a'')$ and $N_2^+(B)$ densities as functions of post-discharge time for the same conditions as in figure 6. The vibrational sources, R20–R23 and R26–R29, are not allowed in this case. Only R19 and R30 are allowed.

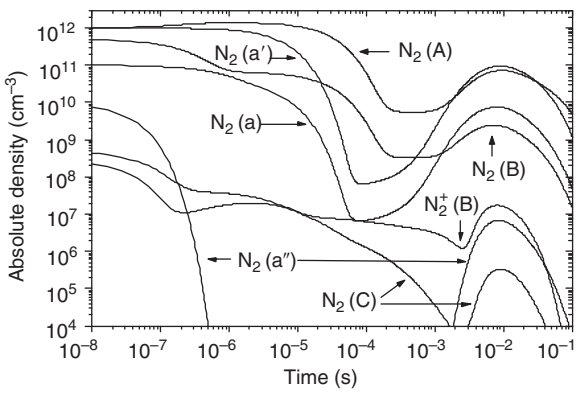

Figure 9. The same as in figure 8 with the vibrational sources included.

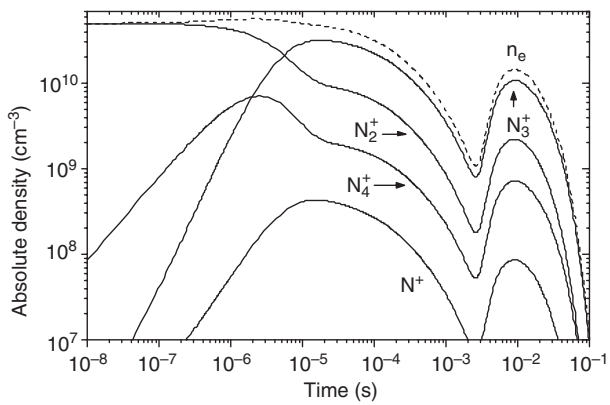

Figure 10. N_{1-4}^+ and n_e densities as a function of post-discharge time for the same conditions as in figure 9.

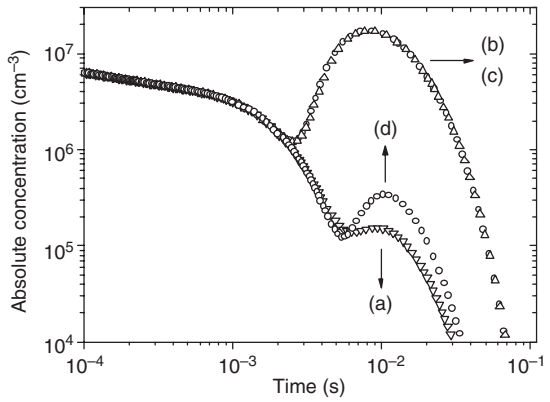

Figure 11. $N_2^+(B)$ density as a function of residence time ($p = 5$ Torr, $\theta = 6000$ K) for some selected groups of vibrational sources. The specification of curves is given in the text.

occurring in the post-discharge. For that, specific groups of processes are selected to describe the different ionization pathways. In figure 11, the $N_2^+(B)$ density is presented as a function of time for several sets of production mechanisms for N_2^+ and N_4^+ ions at $p = 5$ Torr. In curves (a), (b) and (c), the $N_2(a')$ state is produced by the $N_2(X, v > 15)$ pooling reaction (R21):

$$N_2(X, v > 15) + N_2(X, v > 15) \rightarrow N_2(a') + N_2. \quad (1)$$

Then, in curve (a), the N_2^+ and N_4^+ ions are produced by the metastable pooling reactions R24 and R25,

$$\begin{aligned} N_2(a') + N_2(a') &\rightarrow N_2^+ + N_2 + e, \\ N_2(A) + N_2(a') &\rightarrow N_4^+ + e, \end{aligned} \quad (2)$$

in curve (b) by the metastable pooling reaction R27,

$$N_2(a') + N_2(X, v > 24) \rightarrow N_4^+ + e, \quad (3)$$

and in curve (c) by the complete set of ionization mechanisms R24–R29 (table 3). The N_4^+ ions are converted into N_2^+ ones by the mixing reactions presented in table 4 and finally $N_2^+(B)$ is excited via R30:

$$N_2^+(X) + N_2(X, v > 11) \rightarrow N_2^+(B) + N_2. \quad (4)$$

The effect of the ionization pathway (R28) has also been considered:

$$N_2(X, v > 29) + N_2(X, v > 29) \rightarrow N_4^+ + e, \quad (5)$$

which produces the $N_2^+(B)$ temporal profile shown in curve (d). It is clearly deduced from figure 11 that reaction (3) (corresponding to R27 in table 3) is the main source of N_4^+ ions and, consequently, of $N_2^+(X)$ and $N_2^+(B)$ ones. The calculated density ratio of $N_2^+(B)$ at $t \sim 8.5$ ms (maximum value) and at $t \sim 2.5$ ms (minimum value), which is 14 for curves (b) and (c), is near the experimental one as shown in figure 3. Other ionization mechanisms have also been considered as reactions R29 and reactions R20 + R26. However, the maximum values found for $N_2^+(B)$ density are always weaker than those shown in curves (b) and (c).

To conclude, it has been observed that the set of reactions (1) and (3) is the main ionization pathway, between the ones studied here, producing the $N_2^+(B)$ emissions in the pink afterglow.

The mixing reactions presented in table 4 were also studied, and it has been observed that ionic conversion from N_4^+ ions to N_2^+ ones is mainly due to reactions R37 and R38. The consideration of these ionic converting mechanisms permits the increase in the absolute $N_2^+(X, B)$ densities because they balance reaction R35. One will arrive at considerably weaker $N_2^+(X, B)$ densities, in the post-discharge, by disregarding them.

A similar analysis was carried out for $N_2(B, C)$ species, and here we will briefly discuss the dominant mechanisms found. For $N_2(B)$ states, figure 8 clearly expresses the ineffectiveness of reaction R19 to reproduce the experimental behaviour in the SLA (see figure 4). The increase in $N_2(B)$ density occurs by reaction R17 when the $N_2(a')$ state is produced by reaction R21 (reaction (1)). The rise in $N_2(A)$ density follows that for $N_2(B)$, mainly by $N_2(B)$ quenching reaction R7, which has a frequency one order of magnitude greater than the spontaneous emission process R9. However, it should be mentioned that reaction R19 has an important participation when $N_2(A)$ density rises. The possibility to explain the production of the $N_2(B)$ state from the $N_2(C)$ one is quite improbable if one compares reactions R12 and R17 at a residence time corresponding to the maximum density (figure 9). Finally, it was observed that the ion–electron recombination mechanism R44, which generates the $N_2(C)$ states, can partially reproduce the second positive system behaviour observed in the pink afterglow (figure 4). The residence time of the $[N_2(C)]$ maximum is in good agreement with the experimental one. However, the ratio $[N_2(C)]/[N_2^+(B)]$ in the model is weak compared to the experimental one, deduced from the ratio $I_{380.5\,nm}/I_{391.4\,nm}$ at the maximum point, indicating the lack of some source for $N_2(C)$ in the model. It was not explicitly written, but the excitation of $N_2(C)$ is also a stepwise process since it requires ionization steps R21 and R27 to produce N_4^+ ions. $N_2(C)$ formation by electron–ion recombination is proposed in [40] and considered in [41, 42].

The N atoms density temporal profile as a function of pressure is presented in figure 12. The increase of N atoms in the post-discharge regime occurs by means of reaction R23. Moritts [6] has carried out N density measurements into the pink afterglow utilizing a mass spectrometer. He has observed, applying also the optical emission spectroscopy technique, that $N_2(B)$, $N_2(C)$ and $N_2^+(B)$ radiative species present an intensity increase along with the N density in the pink afterglow regime. Moreover, his experimental results show that the higher the pressure, the stronger the N atoms peak. In this sense, the kinetic model presented here is in qualitatively good agreement with the N atoms behaviour observed by Moritts in the N_2 pink afterglow.

It should be emphasized that, at this stage of the work, the set of proposed dominant reactions can explain qualitatively the behaviour of active species in the pink afterglow. However, other mechanisms have to be analysed in detail for a better global comprehension of this phenomenon. Loureiro *et al* [8] present an extensive discussion about some of these mechanisms. Here, we will briefly discuss some of them taking

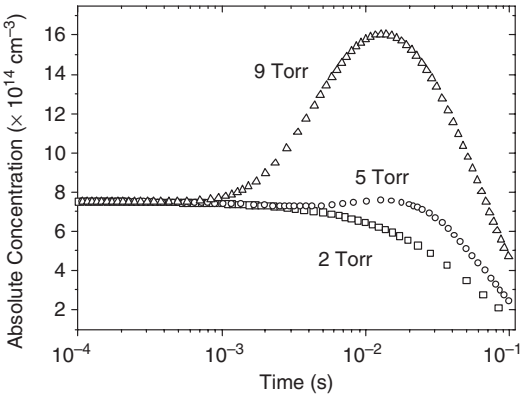

Figure 12. Calculated N atom density as a function of residence time for $p = 2$ Torr and $\theta = 4500$ K (□), 5 Torr and $\theta = 6000$ K (○) and $p = 9$ Torr and $\theta = 7500$ K (△).

into account our calculated VDF. Potential reactions proposed in [8] are

$$N_2(X, v > 24) + N(^4S) \rightarrow N_2(A) + N_2, \quad (6)$$

$$N_2(X, v > 30) + N(^4S) \rightarrow N_2(B) + N_2, \quad (7)$$

$$N_2(X, v > 37) + N(^4S) \rightarrow N_2(a') + N_2. \quad (8)$$

The only reaction that should play an important role in our kinetics is reaction (6) because the other reactions involve too high vibrational levels, which, following our calculated VDF, present too low populations. If reaction (6) produces $N_2(A)$ sufficiently, this should change mainly the dominating pathways to the creation of $N_2(B)$ and $N_2(C)$ states. However, as discussed in [3], this is a spin-forbidden reaction and the reverse process is inefficient [43]. So, in a first analysis this process was discarded. As shown in [3], another important source of the $N_2(A)$ state is the reaction

$$N_2(X, v > 9) + N(^2P) \rightarrow N_2(A) + N(^4S). \quad (9)$$

At the present time, the model cannot account for N atoms in excited states. Therefore, the importance of this mechanism, along with reaction (6) and the influence of the three-body reactions, will be discussed in a future work when the model is implemented to account for N excited states and for temperature gradients in the post-discharge.

6. Comparison of experiment and modelling results

The calculated $N_2^+(B)$ profile and the first negative emission intensity are presented in figure 13 at 5 Torr pressure. Both data were normalized by the peak values. By comparing the experimental and theoretical results, it is found that the theoretical ones are displaced towards lower residence times. Also, the experimental curve is sharper than the calculated one. Nevertheless, the general behaviour qualitatively describes the experiment. Figure 14 shows the comparison between the calculated $N_2^+(B)$ density and the first negative measured intensity (see also figure 5) as a function of pressure, at Z_0 position and 400 sccm flow rate. The model predicts an increase in $N_2^+(B)$ density of about three orders of magnitude as approximately does the experimental curve.

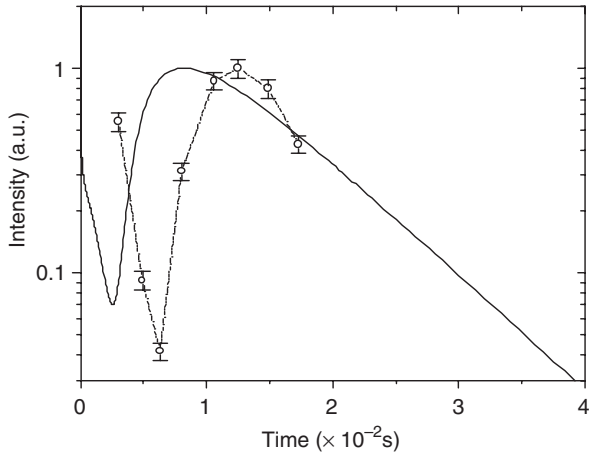

Figure 13. Experimental 391.4 nm intensity (○) and calculated $N_2^+(B)$ density (——) for $p = 5$ Torr, 70 mA current and $Q = 500$ sccm.

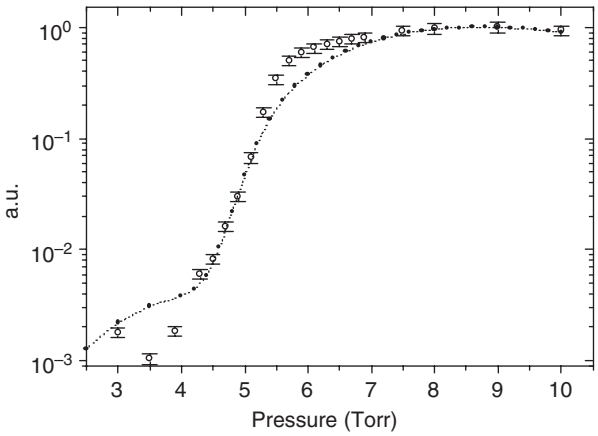

Figure 14. Experimental 391.4 nm intensity (○) and calculated $N_2^+(B)$ density (· · · · · ·) as a function of pressure for a 70 mA discharge current and $Q = 400$ sccm at $z = Z_0$.

7. Conclusion

A DC flowing glow discharge apparatus was constructed, and experimental conditions for the generation of the pink afterglow regime were determined. The emissions of $N_2(B, C)$ and $N_2^+(B)$ radiative states were studied in the post-discharge. The influence of flow rate, pressure and post-discharge position have been considered. The complete pink afterglow phenomenon was kinetically interpreted as dependent on the $N_2(X)$ VDF in the post-discharge region. The last conclusion was based mainly on the strong dependence of post-discharge emissions on the pressure parameter which acts directly on the V–V pumping mechanism and on the residence time of the species.

In order to support the latter affirmations, a kinetic numerical model has been developed. The model requires several entries, among those, the initial electronic density and the discharge vibrational temperature, which were furnished by experimental measurements. Between the assumed processes, one has considered vibrational sources for N atoms, metastable and ionic species (R19–R23 and R26–R30 in tables 2 and 3). The whole set of reactions considered in the simulations

has provided good qualitative agreement between model predictions and experimental behaviour concerning the SLA. In addition, a detailed study of these reactions has pointed out the dominant ones in the SLA generation.

The ionization pathway proposed for the pink afterglow (reactions R21 and R27) should also be considered in N_2 discharges. In fact, considering the discharge VDFs calculated in [16, 38] and the $N_2(a')$ density [38], it is possible to verify that the two-step mechanism, reactions R21 and R27 (see tables 2 and 3), will be dominant in the discharge as compared with the similar one described by reactions R21, R24 and R25. These processes could be investigated with the aid of an N_2–H_2 discharge, where a small admixture of H_2 to N_2can be used as a probe to evaluate the relevant reactions [44]. In this case, the two-step ionization mechanism involving $N_2(X, v > 24)$ states should respond with more sensitivity for H and H_2 species, so that similar electric field behaviour, as described in [45], for N_2–H_2 discharges should take place.

A kinetic process involving $N_2(a')$ metastable and $N_2(X, v)$ species (R23 in table 2) qualitatively reproduced the measured N atom behaviour [5, 6]. A new process for $N_2(C)$ production (reactions R21, R27 and R44 in tables 2–4) was proposed in the N_2 SLA.

This work has provided the description of the pink afterglow phenomenon as a plasma in considering the different ionic species and their interchange reactions.

Acknowledgments

J Levaton was supported by Coordenação de Aperfeiçoamento de Pessoal de Nível Superior, CAPES, Brasília, Brazil. J Amorim was in part supported by Fundação de Amparo à Pesquisa do Estado de São Paulo-FAPESP, under the Young Scientist Program in Emerging Centres (Contract No 96/10475-9).

References

[1] Beale G E and Broida H P 1959 *J. Chem. Phys.* **31** 1030
[2] Supiot P, Dessaux O and Goudmand P 1995 *J. Phys. D: Appl. Phys.* **28** 1826
[3] Sadegui N, Foissac C and Supiot P 2001 *J. Phys. D: Appl. Phys.* **34** 1779
[4] Bromer H H and Hesse J 1969 *Z. Phys.* **219** 269
[5] Diamy A M, Legrand J C, Moritts A and Ricard A 1999 *Surface Coat. Tech.* **112** 38
[6] Moritts A 1997 *PhD Thesis* Université de Paris-Sud, Orsay
[7] Mazouffre S, Foissac C, Supiot P, Vankan P, Engeln R, Schram D C and Sadegui N 2001 *Plasma Sources Sci. Technol.* **10** 168
[8] Loureiro J, Sa P A and Guerra V 2001 *J. Phys. D: Appl. Phys.* **34** 1769
[9] Sa P A, Guerra V, Supiot P and Loureiro J 2001 *Proc. 15th ISPC* **3** 985
[10] Levaton J, Amorim J, Souza A R and Ricard A 2001 *Proc. 15th ISPC* **6** 2143
[11] Blois D, Supiot P, Barj M, Chapput A, Foissac C, Dessaux O and Goudmand P 1998 *J. Phys. D: Appl. Phys.* **31** 2521
[12] Gorbunov N A, Kolokolov N B and Kudryavtsev A A 1988 *Sov. Phys. Tech. Phys.* **33** 1104
[13] Gorbunov N A, Kolokolov N B and Kudryavtsev A A 1991 *Sov. Phys. Tech. Phys.* **36** 616
[14] Press W H, Flannery B P and Vetterling W T 1992 *Numerical Recipes in C: The Art of Scientific Computing* 2nd edn (Cambridge: Cambridge University Press)
[15] Shampine L F and Reichelt M R 1997 *SIAM J. Scient. Comput.* **18** 1–22
[16] Armenise I, Capitelli M, Garcia E, Gorse C, Lagana A and Longo S 1992 *Chem. Phys. Lett.* **200** 597
[17] Cacciatore M, Capitelli M and Gorse C 1982 *Chem. Phys.* **66** 141
[18] Loureiro J and Ferreira C M 1986 *J. Phys. D: Appl. Phys.* **19** 17
[19] Guerra V and Loureiro J 1997 *Plasma Sources Sci. Technol.* **6** 361
[20] Capitelli M, Ferreira C M, Gordiets B F and Osipov A I 2000 *Plasmas Kinetics in Atmospheric Gases* 1st edn (Berlin: Springer)
[21] Nikitin E E, Osipov A I and Umansky C Y 1994 *Reviews of Plasma Chemistry* ed B M Smirnov (New York: Consultants Bureau) p 1
[22] Schwartz R N, Slawsky Z I and Herzfeld K F 1952 *J. Chem. Phys.* **20** 1591
[23] Schwartz R N and Herzfeld K F 1954 *J. Chem. Phys.* **22** 767
[24] Keck J and Carrier G 1965 *J. Chem. Phys.* **43** 2284
[25] Billing G D and Fisher E R 1979 *Chem. Phys.* **43** 395
[26] Guerra V A 1998 *PhD Thesis* Instituto Superior Tecnico, Lisbon
[27] Lagana A, Garcia E and Cicarelli L 1987 *J. Phys. Chem.* **91** 312
[28] Lagana A and Garcia E 1994 *J. Phys. Chem.* **98** 502
[29] Gordiets B, Ferreira C M, Pinheiro M J and Ricard A 1998 *Plasma Sources Sci. Technol.* **7** 363
[30] Guerra V and Loureiro J 1995 *J. Phys. D: Appl. Phys.* **28** 1903
[31] Black G, Wise H, Schechter S and Sharpless R L 1974 *J. Chem. Phys.* **60** 3526
[32] Raizer Y P 1991 *Gas Discharge Physics* 1st edn (New York: Springer)
[33] Santosh K and Ghosh P K 1993 *J. Phys. D: Appl. Phys.* **26** 1419
[34] Loureiro J and Ferreira C M 1989 *J. Phys. D: Appl. Phys.* **22** 67
[35] Lofthus A and Krupenie P H 1977 *J. Phys. Chem. Ref. Data* **6** 113
[36] Ricard A 1996 *Reactive Plasmas* (Paris: SFV)
[37] Nahorny J 1994 *PhD Thesis* Université de Paris-Sud, Orsay
[38] Rajesh N and Ghosh P K 1990 *J. Phys. D: Appl. Phys.* **23** 1663
[39] Kasner W H and Biondi M A 1965 *Phys. Rev.* A **137** 313
[40] Slovetsky D I 1980 *Mechanisms of Chemical Reactions in Non-Equilibrium Plasmas* (Moscow: Nauka)
[41] Simek M, Babicky V, Clupek M, DeBenedictis S, Dilecce G and Sunka P 1998 *J. Phys. D: Appl. Phys.* **31** 2591
[42] Matveyev A A and Silakov V P 1999 *Plasma Sources Sci. Technol.* **8** 162
[43] Clark W G and Setser D W 1980 *J. Phys. Chem.* **84** 2225
[44] Amorim J, Baravian G and Ricard A 1995 *Plasm. Chem. Plasm. Proc.* **15** 721
[45] Ricard A, Gordiets B F, Pinheiro M J, Ferreira C M, Bavarian G, Amorim J, Bockel S and Michel H 1998 *Eur. Phys. J. Appl. Phys.* **4** 87
[46] Piper L G 1988 *J. Chem. Phys.* **88** 6911
[47] Piper L G 1988 *J. Chem. Phys.* **88** 231
[48] Piper L G 1989 *J. Chem. Phys.* **90** 7087
[49] Kossyi I A, Kostinsky A Y, Matveyev A A and Silakov V P 1992 *Plasma Sources Sci. Technol.* **1** 207
[50] Magne L, Cenorgora G and Veis P 1992 *J. Phys. D: Appl. Phys.* **25** 472
[51] Marinelli W J, Kessler W J, Green B D and Blumberg W A M 1989 *J. Chem. Phys.* **90** 2167
[52] Freund R S 1972 *J. Chem. Phys.* **56** 4344
[53] Piper L G 1987 *J. Chem. Phys.* **87** 1625
[54] Wedding A B, Borysow J and Phelps A V 1993 *J. Chem. Phys.* **98** 6227

[55] Gordiets B F, Ferreira C M, Guerra V L, Loureiro J, Nahorny J, Pagnon D, Touzeau M and Vialle M 1995 *IEEE Trans. Plasma Sci.* **23** 750
[56] Polak L S, Sergeev P A and Slovetskii D I 1977 *High Temp.* **15** 13
[57] Guthrie J A, Chaney R C and Cunningham A J 1991 *J. Chem. Phys.* **95** 930
[58] Kaufman F 1969 *Adv. Chem. Ser.* **80** 29
[59] Wei T C, Collins L R and Phillips J 1995 *J. Phys. D: Appl. Phys.* **28** 295
[60] Mehr F J and Biondi M A 1969 *Phys. Rev.* **181** 264
[61] Fitaire M, Pointu A M and Stathopoulos D 1984 *J. Chem. Phys.* **81** 1753